Journal of Magnetic Resonance 214 (2012) 189–199

Contents lists available at SciVerse ScienceDirect

Journal of Magnetic Resonance

journal homepage: www.elsevier.com/locate/jmr

Oscillating gradient measurements of fast oscillatory and rotational motion in the fluids

Igor V. Mastikhin *, Nathan L. Hetherington, Rhys Emms

MRI Centre, Department of Physics, University of New Brunswick, 8 Bailey Drive, Fredericton, New Brunswick, Canada E3B 5A3

ARTICLE INFO

Article history:
Received 11 August 2011
Revised 25 October 2011
Available online 17 November 2011

Keywords:
Oscillatory motion
Fluids
Oscillating gradients
Single-point imaging
Flow
Thermoacoustics
Cavitation

ABSTRACT

We demonstrate the combination of oscillating gradient waveforms with single-point imaging techniques to perform measurements of rapidly oscillating and/or rotating fluid motion. Measurements of Fourier components of motion can be performed over a wide range of frequencies, while the immunity of single-point imaging to time-evolution artefacts allows applications to systems with great susceptibility variations. The processing approaches, displacement resolution, and the diffusive attenuation are analyzed. Measurements of high-speed flow rotation in a spiral phantom, periodic displacements of oscillating gas in a thermoacoustic device and of cavitating liquid reveal a variety of motion spectra. The potential systems for study with the technique include turbulent motion, cavitation, and multiphase flows in general.

1. Introduction

Oscillating and rotating motions are frequently encountered in fluids under high stress. One of the defining characteristics of a turbulent fluid is presence of unsteady vortices of varying sizes and, as a result, the fluid's rotating motion at many frequencies [1,2]. Strong sound in gases will cause oscillations of the gas parcels with the formation of periodic structures [3,4]. In acoustic cavitation, the strong acoustic field generates gaseous bubbles in the liquid; as the bubbles oscillate under the field action, the liquid around them circulates at high frequencies (so-called microstreaming [5]). In a two-phase flow, the combined motion of liquid and gaseous bubbles creates complex flow patterns.

To quantify curvilinear fluid motion, one can perform the measurement of the velocity fields directly (MRI velocimetry). In the case of a homogeneous liquid turbulence, the velocity "snapshots" provide information on the characteristic frequencies and timescales of motion [6,7]. For reconstruction of a curvilinear displacement, a velocity measurement with gradient encoding in all three spatial dimensions is required (see, for example [8,9]). If the direction of the flow velocity changes, it is necessary to perform 2 or 3D velocity encoding and acquisition steps faster than the change duration, imposing stringent requirements on the gradient performance. Susceptibility differences represent a problem for fast frequency-encoding techniques. In many scientifically interesting cases, the fluid motion is coherent, not yet randomized by diffusion, but its spatial scale is below the MRI resolution.

MRI velocimetry is complemented by modulated gradient NMR techniques [10–17] that measure the signal attenuation caused by either randomized dispersive motion or by phase interference of signals from coherently moving spins. Statistically averaged information on the spin motion can be extracted, including the characteristic pore or grain size for flows in porous and granular media. For slowly rotating liquids ("slow" defined as those with the rotation period longer than a pulse sequence execution time), the technique is often combined with velocity field measurements, providing information on vortex sizes and velocities [14,18].

With various gradient modulation approaches available, pulsed field gradients and oscillating gradients are most common. The gradient waveforms employed are designed in such way that their time integral spectra have no zero lobe to exclude the contribution from $D(0)$ to the signal attenuation and to enable measurements of $D(\omega)$. To encode characteristic displacements occurring at short timescales, oscillating gradient waveforms can be advantageous [19–21] as they will require weaker gradients and longer gradient rise times, easing hardware requirements. In addition, they make encoding of a coherent oscillating motion straightforward, as it has been shown in detection of periodic displacements in elastic media (MR Elastography (MRE) [22,23]), granular media [24] and the inner ear's fluid oscillatory motion [25].

Strong magnetic field susceptibility differences in many systems with fast fluid motion (bubble presence in multiphase flow, wires running electric currents of several Amp in thermoacoustic devices),

* Corresponding author. Fax: +1 506 4534581.
E-mail address: mast@unb.ca (I.V. Mastikhin).

1090-7807/$ - see front matter © 2011 Elsevier Inc. All rights reserved.
doi:10.1016/j.jmr.2011.11.003

often accompanied by high dispersion [26] make the use of constant time imaging/single-point imaging techniques [27–29] a necessity. In this work, we combined velocity-compensated oscillating gradient waveforms with single-point imaging techniques (SE-SPI [30] and SPRITE [29]) to measure fast fluid motion in three different media: a model rotating flow (26 m/s, 6500 rad/s), vibrations of gas in a thermoacoustic device, and a cavitating liquid. We focus on two kinds of motion. The first is oscillating motion synchronized with the oscillating magnetic field gradients, as in the gas parcels vibrations caused by the acoustic wave, or in a spatially-resolved rotation of a liquid in a pipe. All parcels of the fluid within the pixel oscillate in phase, and the oscillating gradient technique will yield information on the displacement amplitude directly. The second kind of motion is rotational, as in turbulent fluids or in the granular flow, and is not synchronized with the oscillating gradients. The parcels of the rotating fluid within a pixel oscillate at various phases to the oscillating gradient according to their initial positions. The spin phase interference [14] can be employed to differentiate between different rotation frequencies. As it is not the focus of this work to measure $D(\omega)$, we employ standard sinusoidal oscillations of the gradient to encode the phase contributions.

Scanning the fluid motion by incrementing the oscillating gradient' strength with subsequent Fourier Transform yields a distribution of periodic displacement amplitudes. The Field of Amplitude, conceptually identical to the Fields of View and Flow, is introduced. Its application to diffusive attenuation of the signal permits an estimate of the impact of diffusion on the resolution of periodic motion, helping to choose parameters of the NMR experiment.

The benefits of measuring the fluid motion spectra are illustrated by applying the oscillating gradient technique to studies of an acoustically cavitating liquid for which we extract the information on the local rotation intensity, convert it into the rotational energy spectrum and show how the classical energy power law [31] is modified by the intense interaction of the liquid with the cavitating bubbles.

2. Theory

2.1. Encoding of a synchronized oscillating motion

For spins with the position vector $\vec{r}(t)$ in the presence of the magnetic field gradient $\vec{G}(t)$ after time nT, the NMR signal phase is [32]:

$$\varphi(nT) = \gamma \int_0^{nT} \vec{r}(t) \cdot \vec{G}(t) dt.$$

For a one-dimensional oscillatory motion in x-direction at the frequency ω with the amplitude ξ, the displacement $x(t)$ can be described as

$$x(t) = x_0 + \xi \sin(\omega t),$$

and the signal phase becomes non-zero if the gradient is oscillating synchronously with the motion:

$$\varphi = \gamma \int_0^{nT} \xi G_0 \sin(\omega t) \sin(\omega_g t) dt$$
$$= \frac{1}{2}\gamma \xi G_0 nT \left[\sin c(2n(1-\omega_g/\omega)) - \sin c(2n(1+\omega_g/\omega))\right],$$

where G_0 is the gradient amplitude, $\sin c(x) = \frac{\sin c(\pi x)}{\pi x}$, and the oscillation period $T = 2\pi/\omega_g$.

Ideally, contributions to the signal phase from other frequencies present in the system will be zero: the orthogonality of sinusoidal functions holds when ω is an eigenvalue of ω_g and/or for $n \gg 1$, i.e., for the infinite time integral. The greater n, the narrower the corresponding sinc functions, and the more selective the contribution to the NMR signal phase becomes. At the same time, the diffusive attenuation increases with n so it is often limited by the resolution loss as we discuss later in Section 2.3.

It is convenient to estimate the width of the normalized sinc function by using its Full Width at Half Maximum (FWHM) at $x = 1.21$. For the left sinc in the brackets, we obtain:

$\omega - \omega_g = 1.21\omega/2n$. (Another convenience of using FWHM span is that the integral of the sinc functions in the brackets for their argument values between −0.6 and +0.6 will corrrespond to >99% of the total integral: the contributions from negative and positive regions of sinc functions beyond the FWHM span cancel each other. Therefore, the only contribution to the signal phase will come from the frequency range within the FWHM span.)

For $n = 1$, 2, 3, and 16, FWHM equals correspondingly 0.6, 0.3, 0.2, and 0.07 of the central frequency. For $n = 2$, the smallest number we can use if the velocity compenstaion is required (see Section 2.5), the resulting signal phase will be sensitive to the oscillations in the systems with (angular) frequencies within the range of 0.3ω.

With the understanding of the range of frequencies contributing to the phase, information on the oscillation amplitude can be extracted:

$$\xi = \frac{2\varphi}{\gamma G_0 nT}. \quad (1)$$

This is the principle behind MR-elastography, where the displacement amplitude is further employed in measurements of the elastic modulus of tissues. As the phase can be accumulated over many periods n of oscillation, the sensitivity of the method to a small displacement at a specific frequency can be made quite high.

This technique can be directly applied to the measurements of the oscillatory motion if all parcels oscillate in phase, or if the spatial resolution of the motion is greater than the oscillation wavelength so that regions with different phases can be resolved. Scanning the motion with a range of gradient oscillation frequencies yields Fourier coefficients of fluid's trajectory over the measurement time.

2.2. Field of Amplitude

Eq. (1) assumes that all spins in the voxel oscillate with the same amplitude at the given frequency. In case of a complex fluid motion, we can expect a local distribution of oscillation amplitudes. It is therefore preferable to sample this distribution $\rho(\xi)$ in a manner similar to that of the phase encoding and velocity imaging techniques, by incrementing the phase encoding gradients N times in steps of ΔG from $-G_{\max}$ to $G_{\max}$ with a subsequent Fourier Transform. Introducing $k' = \frac{1}{2\pi}\gamma G T_{\text{total}}/2$, an analog of the regular k-vector, we can describe the sampled signal as

$$S(k') = \int_{-\infty}^{\infty} \rho(\xi) R(k') e^{i2\pi k'\xi} d\xi, \quad (2)$$

where $R(k')$ is the diffusive attenuation function that depends on k' via the gradient strength (here we ignore relaxation terms and the finite sampling size). Then the range of maximum displacement amplitudes will be:

$$2\xi_{\max} = 1/\Delta k = 4\pi/\gamma \Delta G T_{\text{total}},$$

where $T_{\text{total}} = nT$. The amplitude resolution becomes

$$\Delta\xi = \frac{2\xi_{\max}}{N} = \frac{4\pi}{\gamma G_{\max} T_{\text{total}}}. \quad (3)$$

In a direct analogy with the Field of View and Field of Flow definitions, the range $-\xi_{\max} \leqslant \xi \leqslant \xi_{\max}$ can be called the "Field of Amplitude", with negative amplitudes indicating oscillations out

of phase with the oscillating gradients. The Field of Amplitude will remain the same as long as the total oscillation time $T_{total} = nT$ and the maximum gradient strength are fixed, no matter what oscillation frequencies are employed.

2.3. Diffusive attenuation and resolution

For a fluid motion in the presence of magnetic field gradients, the diffusive attenuation needs to be evaluated as the diffusion can be quite high in liquids and gases in particular. Following [11,20], the diffusive signal attenuation function as a function of gradient strength will be $R(G) = \exp\left\{-\frac{3}{8}D\left(\frac{\gamma G}{n\pi}\right)^2 T_{total}^3\right\}$.

We can re-write $R(G)$ in terms of k' and the gradient step number j,

$-N/2 \le j \le N/2$:

$$R(j) = \exp\left\{-\frac{3}{8}D\left(\frac{\gamma\Delta G}{n\pi}\right)^2 T_{total}^3 J^2\right\} = \exp\{-6Dk'^2 T_{total}/n^2\}. \quad (4)$$

The attenuation will depend on the oscillation frequencies: the higher the frequency, the greater n for a fixed T_{total}, and the smaller the attenuation will become. The attenuation is also a function of the gradient step, leading to the modulation of the sampling space $S(k')$ in (2). If the attenuation is strong, it will cause a filter-like effect and lead to a resolution loss.

The resolution loss condition can be defined as the condition when $FWHM_{diff}/FWHM_k > 1$, where $FWHM_{diff}$ is the Full Width at Half Maximum of the Fourier image of the diffusive attenuation function $R(j)$ and $FWHM_k$ is the sampling window resolution [27,33]. $FWHM = 1.21\Delta\xi$ due to finite sampling size. Using (3) and the expression for FWHM of Gaussian function, we obtain:

$$\frac{FWHM_{diff}}{FWHM_k} = 1.08\frac{\sqrt{DT_{total}}}{n\Delta\xi} > 1,$$

or equivalently, $T_{total} > 0.86n^2\Delta\xi^2/D$. The minimum $n = 2$ due to the need for velocity compensation discussed below in Section 2.3,

$$T_{total} > 3.43\Delta\xi^2/D. \quad (5)$$

Assuming no restriction or preferred directions for the stochastic fluid motion, we can use Einstein's equation for isotropic diffusion: $\langle\delta x_{diff}^2\rangle = 2DT_{total}$ where $\langle\delta x_{diff}^2\rangle$ is the mean square diffusive displacement during time T_{total}. Combining this with expression (5), we obtain

$$2.6\Delta\xi < \sqrt{\langle\delta x_{diff}^2\rangle},$$

an intuitively expected result: resolution loss occurs when the random displacement over the total measurement time exceeds the peak-to-peak periodic displacement.

In Fig. 1, Eq. (5) is plotted as the resolution vs. the total gradient oscillation time for three values of dispersion in the fluid systems measured in this paper: $D = 4.2$ cm^2/s (the oscillating/rotating water flow in a glass phantom), 0.1 cm^2/s (Freon-116 in the operating thermoacoustic device), and 10^{-4} cm^2/s (the acoustically cavitated water sample), with the regions of resolution loss below the corresponding lines.

2.4. Encoding of the rotational motion

When the spatial resolution of the motion is such that there is a non-random phase distribution within an image pixel, the phase interference takes place [14]. For a parcel of the fluid with a density ρ rotating in a circle of a radius ξ with a period of rotation $T = 2\pi/\omega$,

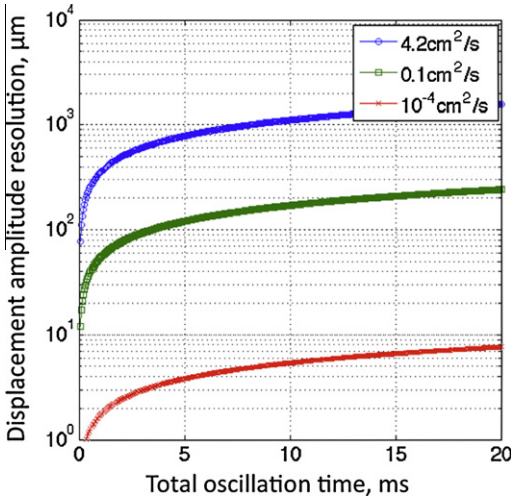

Fig. 1. Periodic displacement amplitude resolution limited by the diffusive attenuation (Eq. (5)) as a function of the total oscillating gradient duration T_{total} calculated for values of dispersion in fluid systems measured in the paper: 4.2 cm^2/s for rotating flow, 0.1 cm^2/s for oscillating gas, 10^{-4} cm^2/s for cavitating liquid. Employed T_{total} were 0.5–5 ms, 4.9 ms, and 16 ms correspondingly. Regions below the lines are those where diffusion-induced blurring overcomes the resolution.

and the magnetic field gradient oscillating at the same frequency ω, the NMR signal phase can be calculated as follows:

$$\varphi_{osc} = \gamma\int_0^{nT}\xi\sin(\omega t+\psi)G_0\sin(\omega t)dt = \frac{1}{2}\gamma\xi G_0 nT\cos\psi, \quad (6)$$

where ψ is the phase shift between the two oscillations. Representing the rotating fluid as a thin ring (see Fig. 2), we integrate over all possible phase shift values to obtain the resulting NMR signal as a function of the gradient strength amplitude:

$$S(G_0) \propto \rho\int_0^{2\pi}\exp\left(i\frac{1}{2}\gamma\xi G_0 nT\cos\psi\right)d\psi = 2\pi J_0\left(\frac{1}{2}\gamma\xi G_0 nT\right)\rho,$$

where J_0 is the Bessel function of the 1st kind. (Here we assume that the fluctuations in the rotation frequency of the fluid are insignificant and occur on the longer timescale than the measurement time.) Thus, even though the sample components undergo coherent motion, the total signal magnitude decays as the gradient increases. Also, when the gradient frequency is different from ω, the integral in (6) is zero. Since $J_0(0) = 1$, NMR signal will be constant for all gradient frequencies different from the frequency of the motion. Therefore,

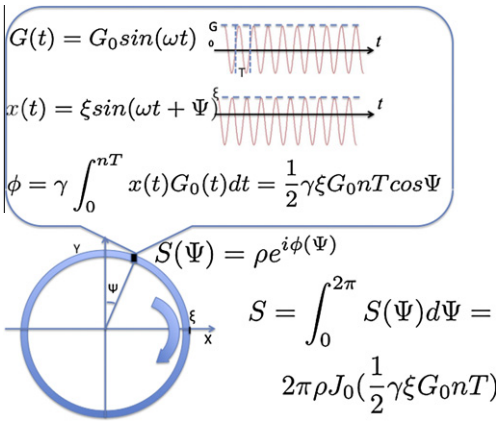

Fig. 2. Phase accumulation for spins oscillating at the same frequency as the magnetic field gradients. The distribution of oscillation phases along a rotating ring results in the NMR signal proportional to Bessel function of 1st kind with its argument being the integral of the displacement and gradient over oscillation time.

the selectivity of the oscillating gradient technique is preserved: the sample regions undergoing rotating motion at the same frequency as that of the applied gradients will be identified by NMR signal modulation. Since the Bessel function of the 1st kind is an even function, the sign of a does not matter, and the sense of rotation will be lost.

When there is a distribution of rotation radii at a given frequency, with a corresponding distribution of Bessel functions (Fig. 3), one can use the Fourier Transform to obtain the Field of Amplitude. The Fourier Transform of a Bessel function of the 1st kind is:

$$\int_{-\infty}^{\infty} AJ(ax)e^{-i2\pi kx}dx = A\frac{\Theta(2\pi k+a)-\Theta(2\pi k-a)}{\sqrt{a^2-(2\pi k)^2}},$$

where Θ is the Heaviside step function [34]. The parameter a is squared so that it will produce a discontinuity both at the positive and the negative values of k (see the Fourier Transform of $J_0(ax)$ for $a = 1$ in the Inset in Fig. 3B), unlike for the imaginary exponential where the sign of the frequency is uniquely defined, facilitating a separation of oscillating and rotating contributions to the NMR signal.

Other differences from FT of imaginary exponentials are: (a) As $FT(J_0(ax = 0)) = 1/a$, the zero line will be affected, and (b) the further the line, the smaller its intensity will become, requiring an additional postprocessing to extract weights A. In Fig. 3A, the Bessel function of the 1st kind multiplied by the diffusive attenuation term with the offset $J_0(ax)\exp(-bx^2) + 1$ is calculated for the values of the parameter a from 0.1 to 1.6, with x increasing from 0 to 63; $b = 2.8 \times 10^{-4}$. Its Fourier Transform, shown in Fig. 3B, demonstrates the symmetric locations of the spectral peaks of the Bessel function corresponding to the values of the parameter a. In a practical experiment, the line width will also be determined by the diffusive attenuation.

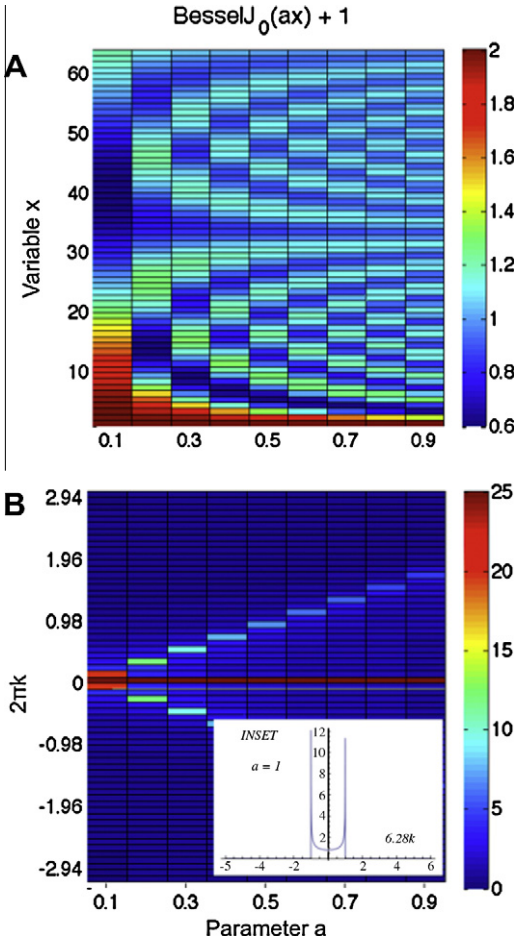

Fig. 3. (A) Calculated values of Bessel function with an offset: $J_0(ax) + 1$ for the parameter a changing from 0.1 with a step of 0.2, and the variable x changing from 0 to 64. (B) The Fourier Transform of the $J_0(ax) + 1$. The central line corresponds to the constant offset and has the intensity of 64. The colorscale was normalized to show better the decreasing peak intensities as the parameter a increases. The vertical coordinate is the values of the wave vector $2\pi k$.

Another possible approach to extracting the distribution might be the use of the orthogonality of Bessel functions [35] as defined on an interval $[0,a]$ for $m \neq n$:

$$\int_0^a J_\nu\left(\alpha_{\nu m}\frac{\rho}{a}\right)J_\nu\left(\alpha_{\nu n}\frac{\rho}{a}\right)\rho d\rho = 0.$$

One can envision using a set of Bessel functions to integrate with the original signal to extract information on the argument. However, the required weighting by ρ will lead to the increased contribution of the non-Bessel component (i.e., the signal from the non-rotating fluid), complicating the analysis.

2.5. Flow contribution and its compensation

Fluids under stress will flow so the spins' position must be in general described as:

$$x(t) = x_0 + vt + \xi\sin(\omega t), \tag{7}$$

where v is the steady velocity in the direction of the gradient. The application of the oscillating gradient to the steadily moving spins will also generate a phase shift:

$$\varphi_{\text{flow}} = \gamma\int_0^{nT} vtG_0\sin(\omega t)dt = -\gamma G_0 n v T^2/2\pi.$$

The flow contribution to the total signal phase becomes important when

$$\left|\frac{\varphi_{flow}}{\varphi_{osc}}\right| = \left|\frac{2\gamma G_0 vnT^2}{2\pi\gamma\xi G_0 nT}\right| = \left|\frac{vT}{\pi\xi}\right| = \left|\frac{2v}{v_{osc}}\right| > 1, \tag{8}$$

where the oscillation velocity amplitude $v_{osc} = \xi\omega$. The flow-generated phase becomes greater than the oscillation-generated phase when the flow velocity exceeds half of the oscillation velocity amplitude. For the rotating motion, the flow-generated phase will be the same for all elements of the rotating circle, becoming a multiplier for the Bessel function:

$$S(G_0) = 2\pi\rho J_0[\gamma\xi G_0 nT/2]\exp(-i\gamma G_0 n v T^2/2\pi),$$

i.e., NMR signal will carry information both on the circle's radius of rotation and its linear velocity in the direction of the applied gradient.

To remove the velocity contribution, we used a symmetric gradient waveform as has been done in measurements of acceleration in flowing media [8,36,37]. A modified sinusoidal gradient waveform, with one lobe removed, will be flow-compensated. For use with spin echo sequences such as SE-SPI [30], the 2nd half of the waveform is inverted after a 180-pulse placed at its center. Such a waveform, in addition to encoding the oscillating spins' phase, will also encode the phase for the accelerating spins. Adding the acceleration term $at^2/2$ to (5) and calculating the resulting phase, we will obtain:

$$\varphi_{acc} = \gamma G_0\int_0^{nT}\frac{at^2}{2}\sin\omega t dt = \gamma G_0 a\frac{n^2T^3}{4\pi}.$$

Compare this to the phase accumulation due to the oscillatory motion, as in (1):

$$\frac{\varphi_{acc}}{\varphi_{osc}} = \frac{\gamma G_0 a n^2 T^3}{2\pi\gamma G_0 n T} = \frac{anT^2}{2\pi\xi} = -\frac{a}{a_{osc}}\frac{n}{2\pi},$$

where $a_{osc} = -\xi\omega^2$ is the acceleration of the rotating spins. For the accelerating motion to be strong enough to contribute to the phase of the oscillating motion, the acceleration must be very significant as the accelerations of rotating spins can be very high. In the model system we use in this paper, the rotational acceleration of water is approx. 1.5×10^5 m/s^2.

3. Experimental

All MRI experiments used a Nalorac (Martinez) 2.35 Tesla, horizontal bore superconducting magnet with a Tecmag (Houston) Apollo console. A water-cooled 20-cm i.d. Nalorac magnetic field gradient set was driven by Techron (Elkhart) 8710 amplifiers. Homebuilt quadrature birdcage ^{1}H and ^{19}F RF coils were driven by a 2 kW AMT (Brea) 3445 RF amplifier.

3.1. ^{1}H MRI of water flow in the spiral phantom

To produce a controlled oscillating/rotating flow motion, a 4-mm o.d., 3 (0.1)-mm i.d. glass tube was formed into a spiral with 10 circular turns of the 12 mm o.d. and a total length of 5 cm (see Fig. 4A). The return end of the tube passed through the spiral's center. The tube was then connected via a pressure regulator to the tap water supply and placed inside the MRI scanner so that its length was aligned with *Z*-direction. The flow rate was measured gravimetrically. The detection of the flow-generated acoustic noise in the phantom was performed with a piezo microphone (SensorTech, ON) attached to the phantom and connected via a preamplifier to a digital scope with 2 μs sampling time and acquisition window of 5 ms; the spectrum is shown in the inset to Fig. 6B.

The MRI velocimetry measurements used the straight segment of the tube return end, as it was easy to differentiate from the spiral segment due to the velocity's opposite sign. To obtain the flow velocity distribution, a SE-SPI sequence with a Pulsed Field Gradient velocity sensitisation was employed with the parameters as follows: Δ = 0.5 ms, Δ = 1.2 ms, the maximum gradient strength of 1.32 G/cm and 32 steps of the gradient increment. The data were Fourier Transformed and then normalized to obtain the displacement propagator.

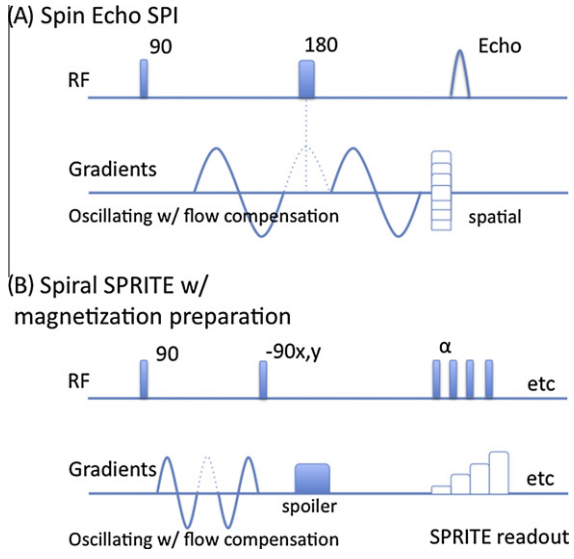

Fig. 4. (A) The glass tube phantom and (B) the measured phase shift in the flowing water, recalculated into the rotation radius for oscillation periods of 1, 3, and 5 ms. The spatial resolution in *Z*-direction is 1 mm.

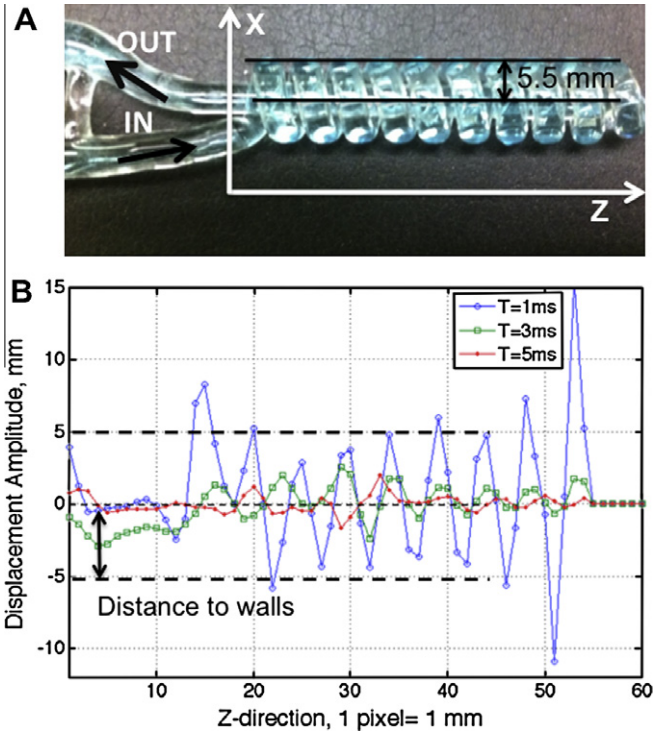

Fig. 5. The pulse sequences with oscillating gradient waveforms: (A) SE-SPI and (B) magnetization-prepared SPRITE with a flip-back pulse. The oscillating gradient waveforms are flow-compensated thanks to the removal of the half-period lobe (its location shown in a dotted line).

To measure the oscillating/rotating motion, a Spin Echo SPI sequence with the oscillating gradient waveform on either side of the 180-pulse was designed (Fig. 5A). The velocity-compensated version of the sequence had half-period of the waveform removed; the non-compensated version did not.

For the detection of the rotating phase distribution along the spiral tube, spatial encoding in the *Z*-direction was added, with 64 points, an encoding time of 0.5 ms and a spatial resolution of 1 mm. The spatial encoding took place immediately before the signal acquisition to reduce the time-of-flight effects. The magnetization recovery delay was 100 ms. Two periods of a sinusoidal gradient were applied in the *X*-direction. The oscillation periods were incremented from 0.5 ms to 10 ms. To circumvent a possible distortion of the sinusoidal gradient waveform by the power amplifier at the low gradient strength, measurements were performed at two gradient strengths: 1.0 G/cm and 1.07 G/cm instead of a single measurement of 0.07 G/cm. The phase difference between the two datasets was then utilized in subsequent calculations.

For the model measurements of the signal from a rotating liquid, the spatial encoding was switched off. The *X*-gradient strength was incremented from 0 to 1.5 G/cm in 64 steps. The oscillation period was incremented from 0.5 ms to 5 ms in 0.5 ms steps.

3.2. ^{19}F MRI of gas in a prototype of a thermoacoustic (TA) device

To measure the periodic displacements of gas in a strong acoustic field, the prototype of a TA device (Applied Research Laboratory, Penn State University, State College) was built. It consisted of a glass tube, a porous (~1 mm diameter channels) and an acoustically transparent heat exchanger ("the stack") heated by a 5A current supply to generate a temperature gradient and induce the oscillations of gas. The sound intensity of >137 dB at 400 Hz was

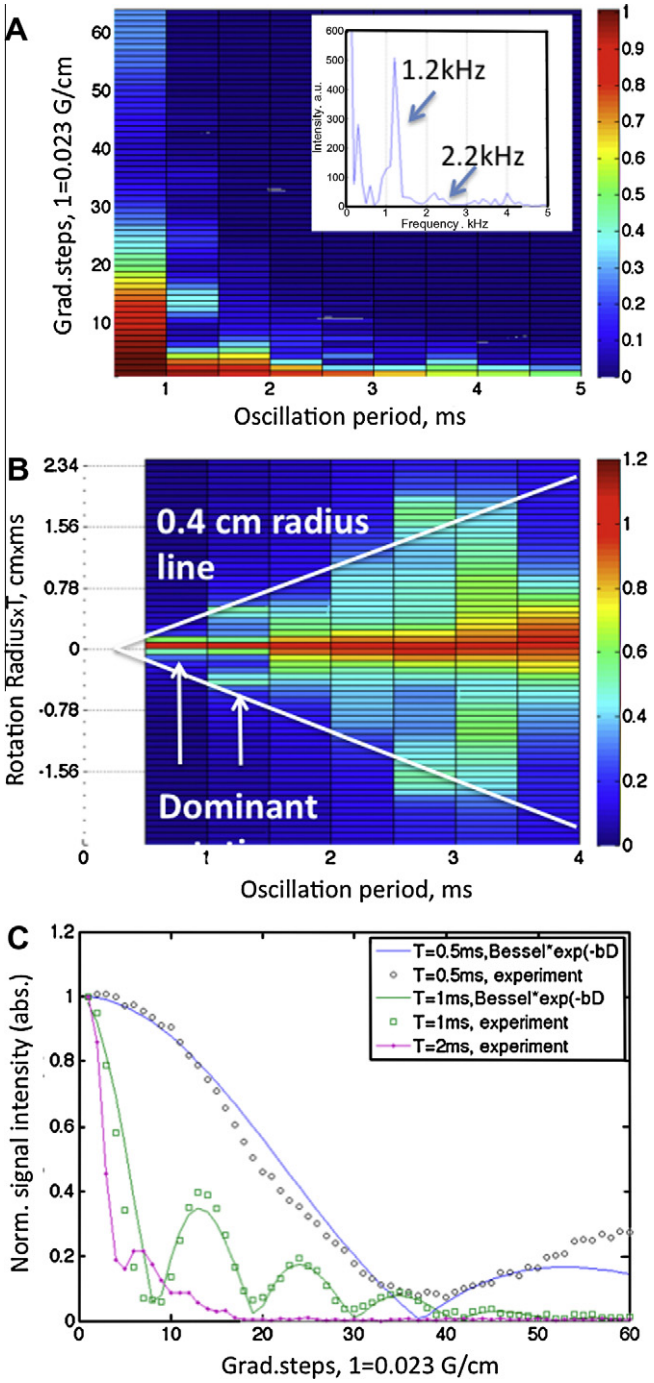

Fig. 6. (A) The magnitude of measured NMR signal from the water flowing in the spiral phantom for the gradient increment of 0.023 G/cm (vertical coordinate) and gradient oscillation period from 0.5 to 5 ms (horizontal coordinate). The inset shows the spectrum of the acoustic noise generated by the flow. (B) FT of (A), with the rotation radius $^*T$ from 0 to 2.34 cm ms (vertical coordinate). Peaks at $T = 0.5$ and 1 ms correspond to the dominant rotations in the phantom. All spectral intensities are normalized by the central line intensities to show the diffusive blurring that increases with T; otherwise only data for first $3T$ would be visible and (C) the signal magnitude for $T = 0.5$, 1, and 2 ms.

measured with a sound level meter (type 2230, Bruel&Kjaer) at 2 cm from the open end inside the tube filled with air.

To keep a fluorinated gas (Freon-116) inside during operation and satisfy the open-end requirement, the prototype was modified: a second, identical glass tube was added to the first one, turning the system into a double Helmholtz resonator. The resulting apparatus, with the current applied, generated sound at a fundamental frequency of 203 Hz.

For MRI experiments, the apparatus was placed inside a ^{19}F RF coil in the MRI scanner. The velocity measurements were performed on the operating device with the SE-SPI sequence, as above, with the parameters as follows: $\Delta = 0.5$ ms, $\Delta = 2.9$ ms, the maximum gradient strength of 14 G/cm and 32 steps of the gradient increment.

Measurements of oscillatory motion in gas were performed with the SE-SPI sequence with oscillating gradients (Fig. 5A) with eight scans and a recovery delay of 50 ms. Spatial encoding along the Z-direction (64 points) was accomplished with a gradient pulse of 0.2 ms duration, resulting in 2 mm resolution. Gradient oscillations were performed at frequencies $\nu = 203$ Hz (the fundamental ν_0), 406 and 612 Hz, with two oscillation periods. Oscillating gradients were incremented in nine steps from −5.6 G/cm to 5.6 G/cm, with the displacement amplitude resolution (3) of 180 μm. The synchronization of the pulse sequence with the sound wave was done with an acoustic microphone placed inside the prototype. The microphone output was connected via a homebuilt trigger to one of the TTL lines of the Tecmac Apollo console.

3.3. ^{1}H MRI of cavitating water

Cavitation experiments were performed with the following experimental setup (Fig. 8A): a magnetostrictive ultrasound transducer (Industrial Sonomechanics, NY) with a sapphire horn operated at 19.1 kHz. The sapphire horn was immersed in a water solution-filled plastic cuvette (4 cm diameter, 15 cm long) placed inside the MRI scanner and oriented along its Z-direction. The distance between the tip of the horn and the cuvette's end was 7.8 cm, corresponding to 1 wavelength of the ultrasound in water at the US frequency of 19.1 kHz, providing the standing-wave condition. Water solution contained [$MnSO_4$] = 0.2 mM. The acoustic pressure of 3.8 Atm was measured by a hydrophone at the end of the cuvette.

For the detection of the rotating motion in the cavitating liquid, a magnetization-prepared spiral SPRITE sequence [38] with Z-storage was designed (Fig. 5B). A 90-pulse was followed by the sinusoidal gradient for duration of 16 ms. After that, −90 X-pulse converted the prepared magnetization into the longitudinal magnetization, with a subsequent spoiler gradient to dephase the remaining transverse magnetization. 10 ms later, a spiral SPRITE sequence was run to read out the longitudinal magnetization. The parameters of the spiral SPRITE sequence: FOV = 20 cm(Z) × 17 cm (X), 64 × 64 points, 5 s acquisition time with a single scan. The sequence was repeated with −90 Y-pulse for purpose of the signal phase extraction.

The measurements were done with 16 values of the oscillating gradient frequency, from 62.5 Hz to 1 kHz, with the 62.5 Hz increment. The gradient strength was 11 G/cm.

4. Results and discussion

4.1. Control flow inside the glass spiral tube – Z-direction

The water flow velocity in the glass tube was measured both with the velocity-sensitized SE-SPI (TE = 1.4 ms) and gravimetrically before and after the experiments with the oscillating gradients. The velocity propagator measurements of the return segment of the tube yielded an average velocity of 18.2 (18) m/s, with the dominant velocity component at 25.5 m/s (with 37% at 28.5 m/s, 32% at 26.1 m/s), taking ~1 ms to complete one rotation.

At such speeds, the water passed through the whole phantom within 10 ms so, as the echo times in our oscillating gradient

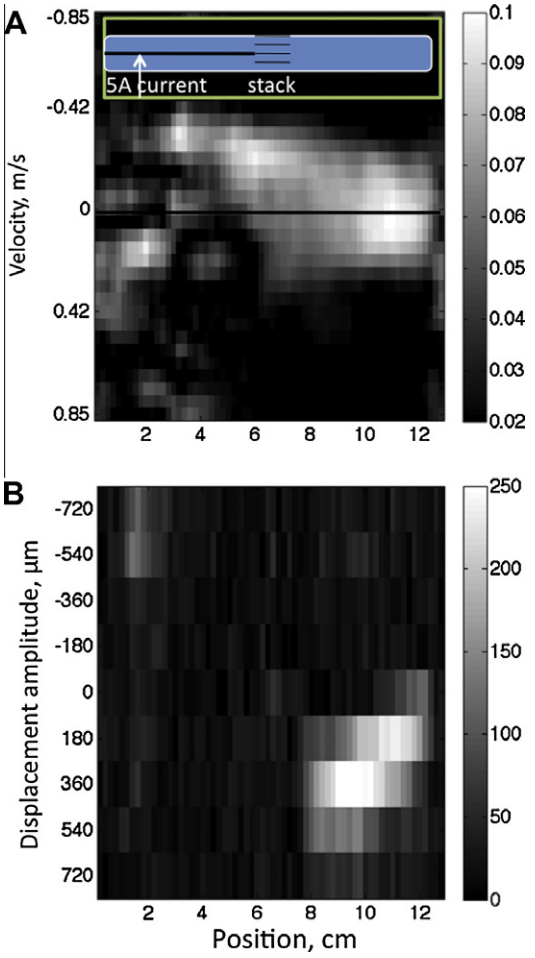

Fig. 7. (A) The schematic of the TA setup (above) with the velocity propagator-position MRI map of operating TA device, velocity as the vertical coordinate and the position as the horizontal coordinate. Both velocity and position are in *Z*-direction and (B) periodic displacement vs position (both along *Z*) during operation. Displacement is positive (in phase with sound oscillations).

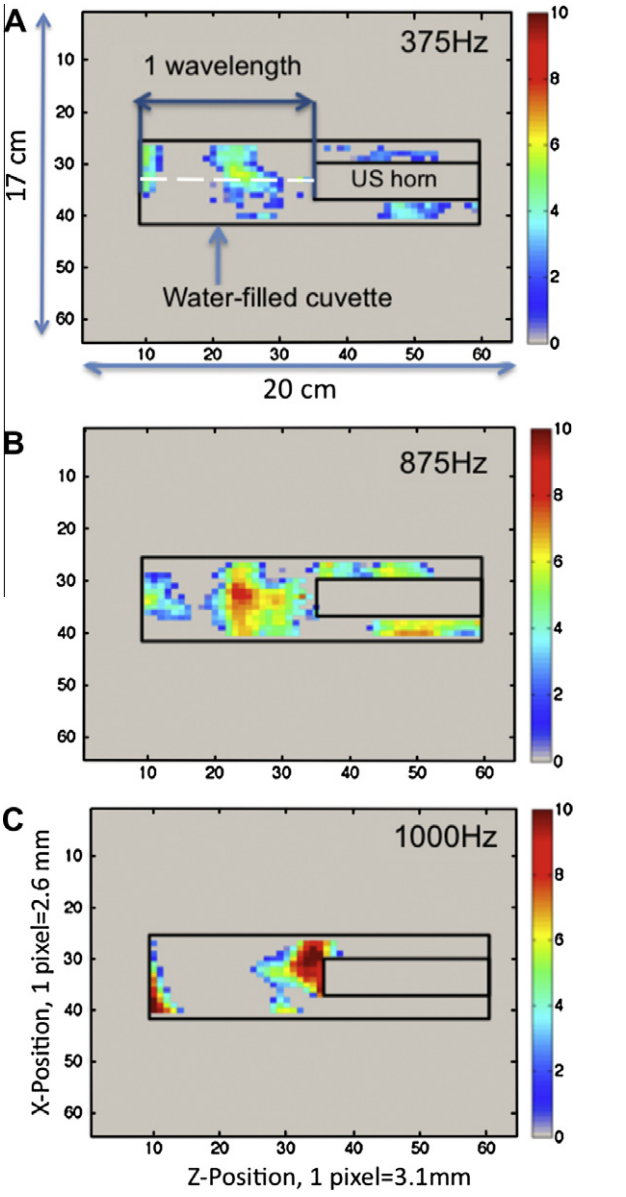

Fig. 8. Fourier coefficients in cavitating water for various gradient oscillation frequencies: 375 Hz (A), 875 Hz (B) and 1000 Hz (C). The vertical axis is the *X*-coordinate, the horizontal axis is the *Z*-coordinate, both in cm. The color scale is in μm. The maximum rotation occurs at the pressure antinodes.

experiments increased with the oscillation periods *T*, the signal intensity decreased as $[1 - V_z(n + 0.5)T/L]$, where *L* is the phantom length (5 cm) and V_z is the water speed along *Z*-direction.

The flow apparent dispersion coefficient was 4.2 ± 0.2 cm^2/s, which was attributed to an elevated turbulent dispersion: for the given system parameters, the Reynolds number $Re = 8 \times 10^4$, and the flowing water undergoes a highly turbulent motion.

To measure the signal phase distribution along the *Z*-direction, measurements with two values of oscillating gradient strengths and 10 oscillating frequencies (all velocity-compensated) with an additional spatial encoding along *Z* were performed, and the phase difference was extracted. The displacement amplitude, shown in Fig. 4B, was calculated according to (1).

The number of maxima does not correspond to the number of turns due to the fast water motion: as the encoding takes 2.5 oscillation periods, the water passes through several turns before being spatially encoded and its signal detected. For the gradient oscillation period of 1 ms, close to the expected rotation period of the water flow, two turns are passed before the data are acquired; the offset of the inflow pipe from *X*-direction generates an extra maximum. The measured displacement varied between −5 and 5 mm, according to the distribution of spins along the turns during the oscillating gradient encoding (see Fig. 2): if at that moment, the spins' *X*-coordinate is positive, they will acquire a positive phase, if it is negative, the phase will be negative as well.

For longer oscillation periods, the displacement was smaller, indicating smaller rotation amplitudes (a motion closer to the inner walls) for spins participating in the slower motion.

4.2. Control flow inside the glass spiral tube – bulk measurements

The above measurements were repeated with *Z*-encoding gradient switched off, and the bulk NMR signal was acquired from the water rotating in the glass phantom as a model of a turbulent vortex. Incrementing the gradient strength and oscillation period, we have scanned a rotation parameter space (the signal magnitude, normalized by $S(G = 0)$ for $T = 0.5$ ms, is shown in Fig. 6A). The zero gradient data point corresponds to the bulk signal with no modulation and it steadily decreases as *T* increases due to the time-of-flight effect: by $T = 5$ ms, half of the phantom is emptied. The dispersion-driven attenuation additionally decreases the signal intensity, as the oscillation period increases (3).

The Bessel-like oscillations of the signal intensity were noticeable for several oscillation period datasets. The magnitude of the signal intensity for $T = 0.5$, 1, and 2 ms was normalized by their zero gradient intensities and plotted in Fig. 6C. The fitting was performed using $J_0(ax) \times \exp(-bD)$, where b was calculated using (3) and the D was the measured value of 4.2 cm^2/s.

For $T = 1$ ms, the fit value of a was 0.286 ± 9 which implies a rotational radius of 0.44 ± 0.01 cm. By using the offset of the Bessel-like signal from the zero line and correcting for the diffusive attenuation, we obtained 94% for the fraction of water rotating with these parameters. This, plus the rotation radius approx. equal to the tube inner radius, indicates that we get the signal from the dominant component of the plug flow. For the given rotation period, we get the water flow velocity of 27 (0.8) m/s, which is higher than the average velocity measured in the straight segment of the tube (~25.5 m/s). It does, however, correspond to the dominant velocity range of 26.1–28.5 m/s (69% of the total flow). To explain the fraction increase, we performed 3D Conical SPRITE imaging of the phantom and measured 10 turns' inner dimensions. It was found that during the spiral tube fabrication, the tube was narrowed, causing a flow speed increase compared to the flow inside the straight tube segment.

On our Bessel maps, the signal for $T = 0.5$ ms has a minimum at #39 of the gradient step (Fig. 6C). Fitting it with a Bessel function results in $a = 0.064 \pm 9$, with the rotation radius of 0.17 ± 3 cm, with 87% of participation for the water flow. We attribute this to the rotation inside the spiral tube itself that has a diameter of 0.14–0.15 cm. Another indication that the detected rotation has a different physical origin is the signal's weaker diffusive attenuation: the fitted line on the figure was calculated using the measured bulk diffusion coefficient value. The rotations along x at 0.5 and 1 ms permit a reconstruction of the spiral fluid motion inside the phantom. They also agree with the acoustic noise spectrum dominated by two main frequencies at 1.1 and 2.1 kHz (inset in Fig. 6B).

The Fourier Transform of the acquired data was performed in the direction of the increasing gradient (the vertical direction of Fig 6A). The resulting dataset is shown in Fig. 6B, where the vertical direction is the direction of the rotation radius multiplied by the gradient oscillation period, and the horizontal direction is that of gradient oscillation periods. The spectrum was normalized by the zero line intensities for each oscillation period, as only data for the first four shortest T's would be visible otherwise. The spectrum is symmetric with respect to the zero gradient line that becomes broader due to the diffusive attenuation increasing with the gradient oscillation period. The 0.4-cm line shows the location of the spectral lines corresponding to the average radius of the spiral tube.

The 1 ms period has a well-defined spectral region (radii of 0.39 and 0.46 cm); integration of the line intensities yields 86% of the total amount of water.

Since the flow is turbulent, water parcels undergo a complicated motion. Along with the dominating rotation corresponding to the plug flow, there are other rotations seen on the Figure at longer oscillation periods even though the diffusive broadening becomes very strong. Their apparent contribution to the signal is exaggerated as most of the fast flow leaves the phantom.

4.3. Periodic motion of gas inside the operating TA engine

The T_1-relaxation constant for the stationary gas was measured with an inversion-recovery pulse sequence as 8.1 ± 5 ms. During the TA operation, the NMR signal from the region before the ceramic stack (0–5 cm of position) dropped by a factor of 8 (measured with SPRITE at 0.75 ms encoding time) as soon as the heater was turned on and the sound generation began. We attribute this effect to the thermal demagnetization; the signal loss was also pronounced in velocity and periodic displacement data, leading to noisy propagator. The gas magnetization in the region after the stack was not significantly affected.

Velocity measurements of gas motion in that area during the TA engine operation showed a strong circulation of the gas (the propagator data are spatially resolved along Z, see Fig. 7A), with velocity range from −0.4 m/s to 0.3 m/s. That necessitated the use of velocity-compensated gradient waveforms to measure the periodic displacements. The dominant direction of the flow was against Z (the velocity encoding direction). The oscillating gradient measurements were done both with and without the velocity compensation. The velocity compensation has successfully removed the phase shift caused by the macroscopic flow; only measurements with velocity-compensated gradients are shown.

The dispersion in the region after the stack (7–12 cm of position) was on average 0.1 ± 0.06 cm^2/s. To measure the periodic displacements with the velocity-compensated waveforms, one requires at least two periods of oscillation, with the resulting values of $T_{total} = 9.84$ ms, 4.92 ms, and 2.46 ms for ν_0, $2\nu_0$, and $3\nu_0$. The middle line in Fig. 1 is plotted for $D = 0.1$ cm^2/s. The plot shows that dispersion-mediated blurring begins to overcome 200 μm resolution at total oscillation times about 10 ms, thus making measurements of the fundamental oscillation mode impossible. Therefore, it was decided to measure the displacements at $2\nu_0 = 406$ Hz ($T_{total} = 4.92$ ms) with a displacement amplitude resolution of 180 m.

Measurements of periodic motion are shown in Fig. 7B. The displacement is positive, indicating that it is synchronized with the acoustic oscillations. The displacement amplitudes increase from zero at the tube end to 360–540 μm near the ceramic stack following the half-wavelength standing wave pattern. There are no symmetric peaks on the periodic motion map, meaning the absence of vortices rotating at 406 Hz in gas, which is not surprising as the acoustic streaming proceeds at longer timescales.

We could not find a calibrated microphone capable of operating at high sound intensities and small enough to fit inside the tube. We had to disassemble the device to place a calibrated sound level meter at 2 cm from the open end of the tube with the ceramic stack. The measurements in excess of 137 dB at 400 Hz (the sound meter was operating at the upper limits of its sensitivity) correspond to the periodic displacements amplitudes of 178 μm. At 2 cm from the tube's closed end, the MRI measurements yield 360 μm. The generated sound wave is highly nonlinear and a much greater sound intensity (in excess of 150 dB) can be expected inside the stack region [39]; the work to directly measure the sound is ongoing.

Diffusive attenuation represents a major challenge as it puts lower limits on the range of measurable frequencies. Higher frequencies in thermoacoustic devices mean smaller device sizes that, incidentally, are being actively developed [40,41] as having higher efficiency and ease of harvesting the excess thermal energy due to smaller temperature gradients required for operation. Weaker temperature gradients will also be beneficial for NMR visualization of fluid motion inside the ceramic stack. Other visualization methods applied to studies of acoustic streaming in thermoacoustic devices, such as Particle Image Velocimetry [42], often have to operate with scaled-up replicas due to the methods' technical limitations, are unable to work with smaller-size devices and cannot provide any information on fluid motion inside the porous material.

4.4. Cavitation: vortices in the cavitating liquid

We used a cavitating liquid as a model of a complex fluid motion. The cavitating liquid is characterized by the presence of bubbles that actively interact with the liquid, generating an energy exchange between these two components of the medium [43]. In

acoustic cavitation, bubbles are produced by a sound pressure drop, and they absorb the energy of the acoustic wave via oscillation, growth and a subsequent collapse, depositing that energy into the surrounding liquid.

Depending on spatial and timescale, one will encounter a local circulation of the liquid around the bubbles at their oscillating frequency, or a macro-motion caused by the bubbles moving in the medium (acoustic streaming [44]).

The bubble-filled flows differ from other turbulent flows in many ways, one of which is the spectral energy distribution. As the interaction between the bubbles and the liquid increases, the bubble wakes generate high-frequency terms in the fluid's kinetic energy. As a result, the classic 5/3-power law of the energy spectrum becomes replaced by a 8/3-dependence [31].

The cavitating bubbles tend to accumulate in certain regions of the standing wave: large bubbles congregate near nodes and smaller bubbles near the antinodes of acoustic pressure [45]. (Here "large" is defined as larger than the resonant size defined by the Minnaert formula [46], about 0.1 mm in for the employed frequency). As the bubbles grow or collapse, they get pushed by the gradient of acoustic pressure in the corresponding location, forming streamers. Considering that the lifetimes of most bubbles are on the order of several dozens of acoustic oscillation cycles or less, the resulting motion of bubbles and entrained water is very active.

Our goal was to apply the oscillating gradient technique for detection of vortices in the cavitating liquid. We used oscillating gradients with a flip-back pulse as a magnetization preparation module and the spiral SPRITE sequence as a readout. The 10 ms delay between the preparation and readout will cause an information loss. Moreover, the readout part, consisting of spiral SPRITE, will take several dozens of ms to cover essential regions of k-space, so the effective delay will be even greater, about 100 ms. Nevertheless, with the flow speeds on the order of several cm/s, the change in location between various characteristic areas of the sample will be about 1–5 mm, or 1–2 pixels, which was thought to be acceptable.

The oscillating gradient frequency range was from 62.5 Hz to 1000 Hz: 16 frequencies separated by a 62.5 Hz step. The same sequence was then repeated with the oscillating gradient amplitude set to zero. After the 2D Fourier Transform revealed the spatial information, the datasets were processed by dividing the oscillating gradient datasets' magnitude by the ones with zero frequency, assuming each voxel underwent a rotating motion. The centric SPRITE signal can be presented as:

$$S(x,y) \propto S_{osc}(x,y)e^{-t_p/T_2^*}R,$$

where R includes relaxation terms during the preparation, t_p is the encoding time, and T_2^* is the inhomogeneous relaxation time constant. T_2^* can be sensitive to the presence of bubbles due to the susceptibility effects, but, as the resulting change will be the same both for the oscillating gradients and the zero gradients during the preparation time, the ratio of the two signals will yield:

$$\frac{S(G_0)}{S(0)} = J_0(0.5\gamma\xi nG_0T).$$

The datasets were then processed, and the values of the rotation radii were extracted (shown in Fig. 8A–C).

It is important to note that the diffusive attenuation will *decrease* as $1/n^2$ (2) when the frequency increases for the fixed gradient strength and duration. There is, however, an observable signal attenuation that increases with the frequency. As all other factors are taken care of by the normalization described above, we interpret the increased signal attenuation as the one caused by the rotating motion. The acquired images are 2-Dimensional, and each voxel extends across the cuvette's width. When we calculate the rotation radii in each voxel, the obtained values represent a measure of rotation averaged over the voxel's volume.

There is almost no detectable rotation at the low frequency range (Fig. 8A). As the frequency increases, so does the rotating motion that is the strongest in the regions corresponding to the acoustic pressure antinodes (Fig. 8B and C), indicating a greater displacement of water caused by the bubbles smaller than the resonant size. In the nodes of the acoustic pressure, the rotation is substantially weaker. The shift next to the horn is a possible result of the flow between the preparation and readout as the cavitation-induced flow is the strongest next to the horn.

To better understand the motion in the system, we can estimate the kinetic energy of the rotating water by using the known ω and ξ:

$$K \propto \rho\xi^2\omega^2,$$

where ρ is the density of the liquid. The void fraction of the cavitating liquid $(1-\rho)$ is usually below 10%; besides, the density should not change noticeably as a function of frequency in our measurements so we can consider it constant compared to the squared frequency and displacement.

The kinetic energy was calculated for the region between the cuvette's end and the US horn, and averaged along Y from row #32 to #36 on Fig. 8. The logarithm of the energy is shown in Fig. 9A. There is a noticeable growth of energy with the frequency in the regions of the pressure antinodes, less so in the pressure nodes. The growth continues steadily up to the frequency of

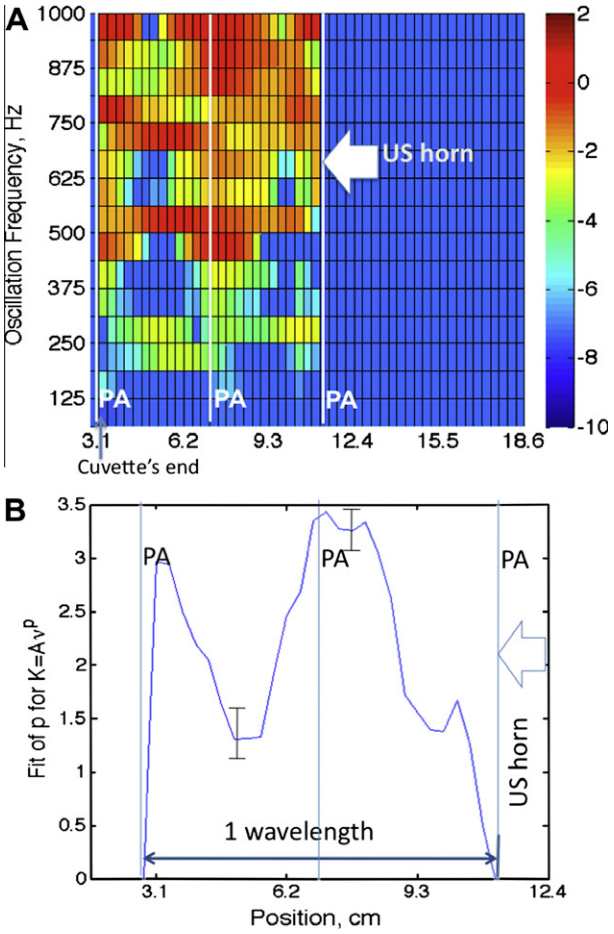

Fig. 9. (A) The logarithm of the kinetic energy of the profile along the dashed line in Fig. 8A (in a.u.). The vertical axis is the gradient oscillation frequency, the horizontal axis is Z-coordinate. (B) Fitted p-values for kinetic energy $K = Av^p$ up to 500 Hz in Fig. 9A. The low p-values are found for the pressure nodes, high values for the pressure antinodes.

500 Hz, after that, the energy levels have a dip, followed by a further increase. It is possible that 500 Hz is close to a characteristic bubble–liquid "interaction frequency" for the given setup.

We used a polynomial fitting for the energy as a function of frequency: $K = Av^p$ for the frequency changing up to 500 Hz. The p-values are shown in Fig. 9B, with the horizontal coordinate being the same spatial position as in Figs. 8 and 9A. According to previous observations [31], the classic 5/3-power law of the energy spectra in the turbulent bubbly liquid becomes replaced by a 8/3-dependence as the interaction between the bubbles and the liquid increases. In our measurements, we observe a similar transition in the p-values from $\sim$1.5 in the pressure nodes, where the interaction between the bubbles and the liquid is reduced, up to $\sim$3 in the pressure antinodes, where the interaction between the bubbles and the liquid is the most intense. Incidentally, the pressure antinodes are also known as regions where the most violent bubble collapses, with emission of light and high chemical activity, take place [45].

5. Conclusion

Combination of oscillating gradient waveforms with single-point imaging techniques proposed here permits measurements of fast fluid motion as it was shown here with a controlled rotating flow system and two applications. Measurement of Fourier components of oscillatory motion can be done at a wide range of frequencies while single-point imaging immune to time-evolution artefacts allows application to systems with great susceptibility variations.

The technique is complementary to fast velocity-mapping techniques: it loses the immediacy of the velocity fluctuations as in [6,7] as its total measurement time is much longer; instead, it samples the statistically averaged information, allowing for a much greater range of sampled frequencies. The technique opens possibilities of investigating coherent motion in fluids at a short timescale, for example, the microstreaming in the vicinity of the cavitating and collapsing bubbles, as long as a fast-switching gradient power amplifier and a low-inductance gradient coil are available.

There are several physical and technical limiting factors. Resolution of the periodic displacement is dispersion-limited, and strong dispersion prohibits measurements of oscillations below the blurring limit as was shown with the thermoacoustic devices. Another factor is the influence of the medium: if the internal gradients generated by the medium are stronger than the oscillating gradient, the signal encoding will be lost as might be the case near pore walls and, in particular, at higher magnetic fields where the susceptibility effects are much higher. The technical factors are the bandwidths of the gradient coil and the power amplifier, i.e. their ability to reproduce the required waveform.

Acknowledgments

The authors would like to thank Brian Malcolm for fabricating the glass phantom and Brian Titus and Murray Olive for fabricating parts of the experimental setup. Fruitful discussions with Drs. Newling and Normandeau (UNB Physics) are greatly appreciated. National Science and Engineering Council of Canada's Undergraduate Student Research Assistant program is gratefully acknowledged (N.H.).

References

[1] L.F. Richardson, Atmospheric diffusion shown on a distance-neighbour graph, Proc. Roy. Soc. London. Ser. A, Contain. Papers Math. Phys. Charact. 110 (1926) 709–737.
[2] A.N. Kolmogorov, The local structure of turbulence in incompressible viscous fluid for very large Reynolds numbers, Proc. USSR Acad. Sci. 30 (1941) 299–303.
[3] G.W. Swift, Thermoacoustic engines, J. Acoust. Soc. Am. 84 (1988) 1145–1180.
[4] S. Backhaus, G.W. Swift, A thermoacoustic Stirling heat engine, Nature 399 (1999) 335–338.
[5] S.A. Elder, Cavitation microstreaming, J. Acoust. Soc. Am. 31 (1959) 54–64.
[6] K. Kose, Spatial mapping of velocity power spectra in Taylor–Couette flow using ultrafast NMR imaging, Phys. Rev. Lett. 72 (1994) 1467–1470.
[7] J.C. Gatenby, J.C. Gore, Echo-planar imaging studies of turbulent flow, J. Magn. Reson. A 121 (1996) 193–200.
[8] A.J. Sederman, M.D. Mantle, C. Buckley, L.F. Gladden, MRI technique for measurement of velocity vectors, acceleration, and autocorrelation functions in turbulent flow, J. Magn. Reson. 166 (2004) 182–189.
[9] A.J. Sederman, M.L. Johns, A.S. Bramley, P. Alexander, L.F. Gladden, Magnetic resonance imaging of liquid flow and pore structure within packed beds, Chem. Eng. Sci. 52 (1997) 2239–2250.
[10] J. Stepisnik, Analysis of NMR self-diffusion measurements by a density matrix calculation, Physica 104B (1981) 350–364.
[11] J. Stepisnik, Measuring and imaging of flow by NMR, Prog. NMR Spectrosc. 17 (1985) 187–209.
[12] P.T. Callaghan, J. Stepisnik, Frequency-domain analysis of spin motion using modulated-gradient NMR, J. Magn. Reson. A 117 (1995) 118–122.
[13] J.D. Seymour, P.T. Callaghan, "Flow-diffraction" structural characterization and measurement of hydrodynamic dispersion in porous media by PGSE NMR, J. Magn. Reson. A 122 (1996) 90–93.
[14] J.D. Seymour, B. Manz, P.T. Callaghan, Pulsed gradient spin echo nuclear magnetic resonance measurements of hydrodynamic instabilities with coherent structure: Taylor vortices, Phys. Fluids 11 (1999) 1104–1113.
[15] P.T. Callaghan, S.L. Codd, J.D. Seymour, Spatial coherence phenomena arising from translational spin motion in gradient spin echo experiments, Concepts Magn. Reson. 11 (1999) 181–202.
[16] P.T. Callaghan, S.L. Codd, Flow coherence in a bead pack observed using frequency domain modulated gradient nuclear magnetic resonance, Phys. Fluids 13 (2001) 421–427.
[17] X. Ren, S. Stapf, B. Blumich, NMR velocimetry in model fixed-bed reactors of low aspect ratio, AIChE J. 51 (2005) 392–405.
[18] S. Jerschow, Thermal convection currents in NMR: flow profiles and implications for coherence pathway selection, J. Magn. Reson. 145 (2000) 125–131.
[19] M. Schachter, M.D. Does, A.W. Anderson, J.C. Gore, Measurements of restricted diffusion using an oscillating gradient spin-echo sequence, J. Magn. Reson. 147 (2000) 232–237.
[20] M.D. Does, E.C. Parsons, J.C. Gore, Oscillating gradient measurements of water diffusion in normal and globally ischemic rat brain, Magn. Res. Med. 49 (2003) 206–213.
[21] E.C. Parsons, M.D. Does, J.C. Gore, Temporal diffusion spectroscopy: theory and implementation in restricted systems using oscillating gradients, Magn. Res. Med. 55 (2006) 75–84.
[22] R. Muthupillai, D.J. Lomas, P.J. Rossman, J.F. Greenleaf, A. Manduca, R.L. Ehman, Magnetic Resonance Elastography by direct visualization of propagating acoustic strain waves, Science 269 (1995) 1854–1857.
[23] R. Muthupillai, P.J. Rossman, D.J. Lomas, J.F. Greenleaf, S.J. Riederer, R.L. Ehman, Magnetic resonance imaging of transverse acoustic strain waves, Magn. Reson. Med. 36 (1996) 266–274.
[24] Lori Sanfratello, Eiichi Fukushima, Robert P. Behringer, Using MR elastography to image the 3D force chain structure of a quasi-static granular assembly, Granular Matter 11 (2009) 1–6.
[25] Winfried Denk, Robert M. Keolian, Seiji Ogawa, Lynn W. Jelinski, Oscillatory flow in the cochlea visualized by a magnetic resonance imaging technique, Proc. Natl. Acad. Sci. USA 90 (1993) 1595–1598.
[26] D.O. Kuethe, Measuring distributions of diffusivity in turbulent fluids with magnetic-resonance imaging, Phys. Rev. A 40 (1989) 4542–4551.
[27] S. Gravina, D. Cory, Sensitivity and resolution of constant-time imaging, J. Magn. Reson. B 104 (1994) 53–61.
[28] B.J. Balcom, R.P. MacGregor, S.D. Beyea, D.P. Green, R.L. Armstrong, T.W. Bremner, Single-point ramped imaging with $T1$ enhancement (SPRITE), J. Magn. Reson. A 123 (1996) 131–134.
[29] M. Sankey, Z. Yang, L. Gladden, M.L. Johns, D. Lister, B. Newling, SPRITE MRI of bubbly flow in a horizontal pipe, J. Magn. Reson. 199 (2009) 126–135.
[30] A.V. Ouriadov, R.P. MacGregor, B.J. Balcom, Thin film MRI – high resolution depth imaging with a local surface coil and spin echo SPI, J. Magn. Reson. 169 (2004) 174–186.
[31] M. Lance, J. Bataille, Turbulence in the liquid phase of a uniform bubbly air–water flow, J. Fluid Mech. 222 (1991) 95–118.
[32] P.T. Callaghan, Principles of Nuclear Magnetic Resonance Microscopy, Oxford University Press, 1993.
[33] P.J. Prado, B.J. Balcom, I.V. Mastikhin, A.R. Cross, R.L. Armstrong, A. Logan, Magnetic resonance imaging of gases: a single-point ramped imaging with T1-enhancement (SPRITE) study, J. Magn. Reson. 137 (1999) 324–332.
[34] M. Abramowitz, I.A. Stegun (Eds.), Handbook of Mathematical Functions with Formulas, Graphs, and Mathematical Tables, Dover, 1972 (9th printing).
[35] G.B. Arfken, H.J. Weber, Mathematical Methods for Physicists, San Diego, 2001.
[36] D.G. Norris, Acceleration imaging by NMR, in: Proc., SMRM. 5th Annual Meeting, London, 1985, p. 593.
[37] Jean-Pierre Tasu, Odile Jolivet, Elie Mousseaux, Annie Delouche, Benoit Diebold, Jacques Bittoun, Acceleration mapping by fourier acceleration-encoding: *in vitro* study and initial results in the great thoracic vessels, Magn. Reson. Med. 38 (1997) 110–116.

[38] M. Halse, J. Rioux, S. Romanzetti, J. Kaffanke, B. MacMillan, I.V. Mastikhin, N.J. Shah, E. Aubanel, B.J. Balcom, Centric scan SPRITE magnetic resonance imaging: optimization of SNR, resolution, and relaxation time mapping, J. Magn. Reson. 169 (2004) 102–117.
[39] S. Jung, K. Matveev, Study of a small-scale standing-wave thermoacoustic engine, Proc. Inst. Mech. Eng. Part C: J. Mech. Eng. Sci. 224 (2010) 133–141.
[40] O.G. Symko, E. Abdel-Rahman, Y.S. Kwon, M. Emmi, R. Behunin, Design and development of high-frequency thermoacoustic engines for thermal management in microelectronics, Microelectron. J. 35 (2004) 185–191.
[41] C. Jensen, R. Raspet, Thermoacoustic power conversion using a piezoelectric transducer, J. Acoust. Soc. Am. 128 (2010) 98–103.
[42] X.A. Mao, A.J. Jaworski, Application of particle image velocimetry measurement techniques to study turbulence characteristics of oscillatory flows around parallel-plate structures in thermoacoustic devices, Meas. Sci. Technol. 21 (2010) 035403.
[43] I.V. Mastikhin, B. Newling, Dynamics of dissolved gas in a cavitating fluid, Phys. Rev. E 78 (2008) 066316.
[44] I.V. Mastikhin, B. Newling, MRI measurements of an acoustically cavitated fluid in a standing wave, Phys. Rev. E 72 (2005) 056310.
[45] T.G. Leighton, The Acoustic Bubble, Academic Press, San Diego, 1997.
[46] M. Minnaert, On musical air-bubbles and sounds of running water, Phil. Mag. 16 (1933) 235–248.